

# Approximate Error Correction for Quantum Simulations of SU(2) Lattice Gauge Theories

Zachary P. Bradshaw<sup>1</sup>

<sup>1</sup>*QodeX Quantum, Chicago, IL, USA*

(Dated: March 31, 2026)

We present a protocol for actively suppressing Gauss law violations in quantum simulations of SU(2) lattice gauge theory. The protocol uses mid-circuit measurements to extract a characterization of the gauge-violation sector at each lattice vertex, resolving both the total angular momentum and magnetic quantum numbers of the violation via a group quantum Fourier transform. Syndrome-conditional recovery operations map the state back to the gauge-invariant subspace through an iterative sweep over vertices, a procedure we call gauge cooling. We show that while the Knill-Laflamme conditions are not generically satisfied at vertices with nontrivial singlet multiplicity, every single-qubit error is detected by the gauge syndrome. We demonstrate gauge cooling on a single-plaquette simulation of the Kogut-Susskind Hamiltonian truncated to the spin-1/2 representation under depolarizing and amplitude damping noise, showing that the protocol restores gauge invariance and improves fidelity at noise rates representative of current superconducting hardware.

The standard model of particle physics [1] relies on non-abelian gauge symmetry as an organizing principle [2]. Quantum chromodynamics [3, 4], the SU(3) gauge theory of the strong interaction, confines quarks into hadrons, drives chiral symmetry breaking, and generates the vast majority of the visible mass in the universe. These phenomena are intrinsically nonperturbative and emerge from the strong-coupling infrared dynamics of the theory in a way that cannot be accessed order by order in the coupling constant. Understanding how confinement and mass generation arise from the underlying gauge dynamics remains one of the deepest open problems in theoretical physics more than fifty years after the formulation of QCD.

Lattice gauge theory [5–9] has provided the most successful first-principles approach to this problem. Monte Carlo sampling of the lattice path integral has yielded precision calculations of the hadron spectrum [10], the QCD equation of state at finite temperature [11, 12], and a wide range of hadronic matrix elements relevant to flavor physics and nuclear structure [13]. Yet there are fundamental questions that classical lattice methods cannot address [14]. Real-time dynamics [15], transport coefficients [16], and the phase structure of QCD at finite baryon density all involve physics that is either inaccessible or severely limited by the sign problem [17] and the Euclidean signature of the lattice formulation. These are not merely technical inconveniences; they represent a hard boundary on what can be learned from classical computation alone.

Quantum simulation [18–22] has emerged as a potentially transformative tool for circumventing these limitations. A quantum device can in principle represent the real-time dynamics of a quantum field theory directly in Minkowski signature, without analytic continuation and without a sign problem [23, 24]. Rapid experimental progress in programmable quantum hardware has brought small-scale demonstrations of lattice gauge theory dynamics within reach [25–27], and theoretical work

has established concrete frameworks for encoding gauge theories into qubit systems [28, 29]. SU(2) lattice gauge theory, the simplest non-abelian gauge theory exhibiting both confinement and asymptotic freedom, provides the natural starting point for this program. Success in this setting would establish the viability of quantum simulation as a tool for nonperturbative gauge theory and lay the groundwork for eventual application to the full complexity of QCD that remains beyond classical reach.

A central obstacle to realizing this program is the preservation of gauge invariance on noisy quantum hardware [25, 30–41]. In the Hamiltonian formulation of lattice gauge theory, the physical Hilbert space is defined by a local constraint at every lattice vertex. Indeed, this constraint is known as a Gauss law and takes the form of a non-abelian generalization of the requirement that electric flux be divergenceless in the absence of charges. On a classical computer, this constraint is either built into the representation or enforced algebraically, but a quantum processor has no such protection [5, 33, 42]. Gate errors and decoherence artifacts drive the state out of the gauge-invariant subspace, and once a gauge violation is introduced it can propagate and accumulate over subsequent time steps. For abelian gauge theories such as U(1), the Gauss law reduces to a set of commuting diagonal constraints that can be monitored with relatively simple measurements [26, 43, 44]. In the non-abelian case the constraints at neighboring vertices do not commute with one another, and the gauge-invariant subspace has a richer structure. Maintaining gauge invariance in a non-abelian simulation is therefore a distinct challenge that must be solved before quantum advantage for gauge theory dynamics can be credibly pursued.

In this letter, we present a protocol for actively suppressing Gauss law violations in quantum simulations of SU(2) lattice gauge theory. Mid-circuit measurements extract a syndrome  $(J, M, N)$  characterizing the gauge-violation sector at each vertex, and a conditional recovery operation maps the state back to the physical sub-

space through an iterative sweep we call gauge cooling. We show that while the Knill-Laflamme conditions are not generically satisfied at vertices with nontrivial singlet multiplicity, every single-qubit error is detected by the gauge syndrome, and the residual physical-subspace errors have a structured Pauli decomposition amenable to further correction by concatenation with a stabilizer code [45, 46]. Our approach refines the symmetry-based codes introduced in [47] by replacing the isotopic syndrome extraction with a finer-grained measurement that provides maximal syndrome information for the recovery step. We demonstrate the protocol on a single-plaquette simulation under depolarizing and amplitude damping noise at rates representative of current superconducting hardware.

Our story begins with a discussion of the lattice gauge theory formulation. Consider a spatial lattice with vertex set  $V$  and oriented edge set  $E$ , and let  $G$  be a compact Lie group. To each edge  $e$ , we associate the Hilbert space

$$\mathcal{H}_e = L^2(G), \quad (1)$$

the space of square-integrable functions on  $G$  with respect to the Haar measure [48, 49]. Matter degrees of freedom may optionally reside on vertices, in which case each  $v \in V$  carries a finite-dimensional Hilbert space  $\mathcal{H}_v^{\text{matt}}$  with a unitary representation  $\rho_v: G \rightarrow U(\mathcal{H}_v^{\text{matt}})$ . The full Hilbert space is

$$\mathcal{H} = \bigotimes_{e \in E} \mathcal{H}_e \otimes \bigotimes_{v \in V} \mathcal{H}_v^{\text{matt}}, \quad (2)$$

and the local gauge group is the direct product

$$\mathcal{G} = \prod_{v \in V} G_v \cong G^{|V|}, \quad (3)$$

where the  $v$  subscript has been added to index the copies of  $G$ .

An element  $\mathbf{h} = (h_v)_{v \in V} \in \mathcal{G}$  acts on an oriented edge  $e$  from vertex  $v$  to vertex  $w$  via

$$U_e(\mathbf{h}) = L_{h_v} R_{h_w}, \quad (4)$$

where  $L_{h_v}$  and  $R_{h_w}$  are the commuting left and right regular representations defined by

$$(L_{h_v} f)(g) = f(h_v^{-1}g), \quad (R_{h_w} f)(g) = f(gh_w). \quad (5)$$

The element  $\mathbf{h}$  also acts on matter via  $U_v(\mathbf{h}) = \rho_v(h_v)$ . Taking the tensor product over all edges and vertices produces a unitary representation  $U: \mathcal{G} \rightarrow U(\mathcal{H})$ . A state  $|\Psi\rangle \in \mathcal{H}$  is *physical* if it is invariant under all local gauge transformations,

$$U(\mathbf{h})|\Psi\rangle = |\Psi\rangle \quad \forall \mathbf{h} \in \mathcal{G}. \quad (6)$$

The physical subspace  $\mathcal{H}_{\text{phys}} \subset \mathcal{H}$  is therefore the  $\mathcal{G}$ -invariant subspace. In the language of representation theory, it is the trivial isotopic component of  $\mathcal{H}$  under the action of  $\mathcal{G}$ .

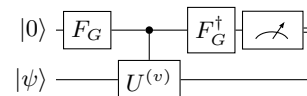


FIG. 1. Circuit for the Gauss law test at a single vertex  $v$ . The ancillary register is prepared in the uniform superposition  $|+\mathcal{G}\rangle = \frac{1}{\sqrt{|\mathcal{G}|}} \sum_g |g\rangle$  by the unitary  $F_G$ . The controlled gauge action applies  $U^{(v)}(g)$  to the data register conditioned on the ancilla state  $|g\rangle$ . The inverse  $F_G^\dagger$  is applied and the ancilla is measured; the outcome corresponding to  $|0\rangle$  is the “accept” outcome, with acceptance probability  $\langle \psi | \Pi_0^{(v)} | \psi \rangle$ .

The projector onto the physical subspace is given by the group average

$$\Pi_{\text{phys}} = \int_{\mathcal{G}} U(\mathbf{h}) d\mathbf{h}, \quad (7)$$

where  $d\mathbf{h}$  is the normalized Haar measure on  $\mathcal{G}$ . Since  $\mathcal{G}$  factorizes over vertices, this integral factorizes as well,

$$\Pi_{\text{phys}} = \prod_{v \in V} \Pi_0^{(v)}, \quad \Pi_0^{(v)} = \int_G U^{(v)}(h_v) dh_v, \quad (8)$$

where  $U^{(v)}(h_v) := U(1, \dots, 1, h_v, 1, \dots, 1)$  denotes the gauge action with  $h_v$  nontrivial at vertex  $v$  only. This factorization is important; it means the symmetry test can be applied locally, one vertex at a time.

By making the projective measurement  $\{\Pi_0^{(v)}, 1 - \Pi_0^{(v)}\}$  at each vertex, a gauge-violating error can be detected. A method for performing this measurement when  $G$  is a finite group can be found in [50–52], and a circuit implementation is shown in Figure 1. However, this information alone is insufficient for active error correction beyond postselecting on the physical outcome, which is computationally expensive [53, 54]. To perform an active recovery operation, we require a syndrome identifying the type of error that occurred without destroying the information in the state of the system, and we now describe how to make such a measurement when  $G = \text{SU}(2)$ .

By the Peter-Weyl theorem, the link Hilbert spaces  $\mathcal{H}_e = L^2(\text{SU}(2))$  decompose as

$$\mathcal{H}_e \cong \bigoplus_{j \in \frac{1}{2}\mathbb{N}_0} V_j \otimes V_j^*, \quad (9)$$

where  $V_j$  is the carrier space of the spin- $j$  irreducible representation (irrep)  $\pi_j$  with dimension  $d_j = 2j + 1$  and  $\mathbb{N}_0$  denotes the nonnegative integers. The normalized Wigner matrices  $\sqrt{d_j} D_{mn}^{(j)}(g) = \sqrt{2j + 1} [\pi_j(g)]_{mn}$ , with  $-j \leq m, n \leq j$ , form a complete orthonormal basis for  $\mathcal{H}_e$ . In practice, the sum over  $j$  is truncated at  $j_{\text{max}}$ , reducing each edge to a finite-dimensional Hilbert space of dimension  $\sum_{j=0}^{j_{\text{max}}} (2j + 1)^2$ . Additionally, each summand  $V_j \otimes V_j^*$  has a physical interpretation. For an oriented edge  $e$ , the factor  $V_{j_e}$  transforms under gauge transformations at the source vertex and  $V_{j_e}^*$  transforms at the target.

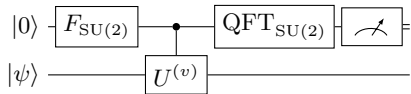


FIG. 2. Syndrome extraction at vertex  $v$ . The circuit is identical to the circuit in Figure 1, except that the inverse preparation  $F_{\text{SU}(2)}^\dagger$  is replaced by the group quantum Fourier transform  $\text{QFT}_{\text{SU}(2)}$ . Measuring the ancillary register in the Wigner basis yields a syndrome  $(J, M, N)$ . The operator applied to the data register selects the component in  $\mathcal{W}_N^J$  and maps it into  $\mathcal{W}_M^J$ , leaving the multiplicity degrees of freedom untouched.

Regrouping the tensor product over edges by vertex and applying the Clebsch-Gordan decomposition (see supplemental material), we obtain the vertex Hilbert space at each vertex  $v$

$$\mathcal{H}_v(\{j_e\}) \cong \bigoplus_{J_v} V_{J_v} \otimes \mathbb{C}^{\mu_{J_v}}, \quad (10)$$

where  $J_v$  labels the total angular momentum at vertex  $v$  and  $\mu_{J_v}$  is the corresponding Clebsch-Gordan multiplicity. Fixing a standard basis  $\{|M\rangle\}_{M=-J}^J$  for  $V_J$ , we define the subspace

$$\mathcal{W}_M^J = \text{span}\{|M\rangle \otimes |\alpha\rangle : \alpha = 1, \dots, \mu_J\} \subset V_J \otimes \mathbb{C}^{\mu_J}, \quad (11)$$

which is the  $\mu_J$ -dimensional subspace of the  $J$ -isotypic component with magnetic quantum number  $M$ . The Gauss law constraint requires that the physical subspace correspond to the singlet sector  $J_v = 0$  at every vertex. The quantum numbers  $J_v$  and the associated magnetic projections together characterize gauge violations at vertex  $v$ , and it is the extraction of these quantum numbers by mid-circuit measurement that enables the active correction protocol we now outline. The implementation proceeds in three steps and is shown in Figure 2.

*Step 1. Prepare the ancillary register.* Ideally, we would initialize an ancillary register in a uniform superposition over the basis for the group algebra generated by  $\text{SU}(2)$ . However, we are typically constrained to finite-dimensional hardware, and so a truncation has to be made. We show in the supplemental material that preparing a uniform superposition over a unitary  $t$ -design is sufficient. Such a superposition has the form

$$\frac{1}{\sqrt{n_t}} \sum_{i=1}^{n_t} |g_i\rangle \quad (12)$$

for some  $n_t$  group elements  $g_i \in \text{SU}(2)$ . The required design strength  $t$  depends on the truncation  $j_{\text{cut}}$  of the group QFT in Step 3 and is discussed in the supplemental material. Note that we may encode the group basis states however we like, so long as the controlled operation in Figure 2 is triggered when the ancillary register is in the state  $|g_i\rangle$  and we perform the final QFT according to this basis assignment.

*Step 2. Apply the controlled gauge action.* Perform the operation

$$\sum_{i=1}^{n_t} |g_i\rangle\langle g_i| \otimes U^{(v)}(g_i), \quad (13)$$

which applies the gauge action  $U^{(v)}(g_i)$  at vertex  $v$  to the data register, conditioned on the ancillary register being in state  $|g_i\rangle$ . After this step, the joint state of the ancilla and data registers for an input state  $|\psi\rangle$  is

$$\frac{1}{\sqrt{n_t}} \sum_{i=1}^{n_t} |g_i\rangle \otimes U^{(v)}(g_i)|\psi\rangle. \quad (14)$$

*Step 3. Apply group quantum Fourier transform.* The quantum Fourier transform can be generalized to a group quantum Fourier transform, where the ordinary transform is recovered by choosing a cyclic group. For  $\text{SU}(2)$ , this operation is defined by

$$\text{QFT}_{\text{SU}(2)} |g\rangle = \sum_{j \in \frac{1}{2}\mathbb{N}_0} \sqrt{2j+1} \sum_{m,n=-j}^j \overline{[\pi_j(g)]_{m,n}} |j, m, n\rangle, \quad (15)$$

which we note acts on an infinite dimensional Hilbert space. Thus, we again run into the finite-dimensional hardware limitation, which we alleviate by truncating the infinite-dimensional QFT along the  $j$  axis. Indeed, we define a cutoff  $j_{\text{cut}}$  so that the truncated version of the QFT acts as

$$\text{QFT}_{\text{SU}(2)}^{\leq j_{\text{cut}}} |g\rangle = \sum_{j=0}^{j_{\text{cut}}} \sqrt{\frac{2j+1}{n_t}} \sum_{m,n=-j}^j \overline{[\pi_j(g)]_{m,n}} |j, m, n\rangle, \quad (16)$$

where  $j$  ranges over half-integer steps and the factor of  $1/\sqrt{n_t}$  is included for normalization purposes. We show in the supplemental material that this truncation is justified. Note that the truncated transform is an isometry from the  $n_t$ -dimensional ancilla register into the subspace spanned by  $\{|j, m, n\rangle : j \leq j_{\text{cut}}, -j \leq m, n \leq j\}$ , and is embedded into a unitary on the full ancilla register by extending to an orthonormal basis in the standard way. A discussion of the relationship between the group algebra basis and the Wigner basis is provided in the supplemental material.

*Step 4. Measure the ancillary register.* Measure the ancillary register in the  $|j, m, n\rangle$  basis, obtaining outcome  $(J, M, N)$ . To determine the post-measurement state of the data register, we substitute the output of Step 2 into Step 3 and project onto the measurement outcome. After the group QFT, the joint state of the ancilla and data registers is

$$\sum_{J,M,N} |J, M, N\rangle \otimes T_{MN}^{(J)} |\psi\rangle, \quad (17)$$

where

$$T_{MN}^{(J)} = \frac{\sqrt{2J+1}}{n_t} \sum_{i=1}^{n_t} \overline{[\pi_J(g_i)]_{MN}} U^{(v)}(g_i) \quad (18)$$

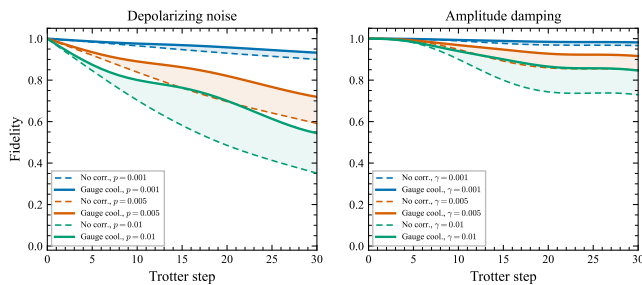


FIG. 3. Fidelity with the ideal noiseless evolution as a function of Trotter step for a single-plaquette SU(2) lattice gauge theory simulation with  $j_{\max} = 1/2$ , coupling  $g^2 = 1$ , total evolution time  $T = 3.0$ , and step size  $dt = 0.1$ . Dashed lines: no error correction. Solid lines: iterative gauge cooling (up to 10 sweeps) applied after each Trotter step. Left panel: qudit depolarizing noise with error rate  $p$  per edge per step. Right panel: amplitude damping with damping rate  $\gamma$  per edge per step.

is the discrete approximation to the operator

$$\sqrt{2J+1} \int_{\text{SU}(2)} \overline{D_{MN}^{(J)}(g)} U^{(v)}(g) dg, \quad (19)$$

which, by the Peter-Weyl orthogonality relations, acts within the  $J$ -isotypic component of  $\mathcal{H}_v$  as

$$T_{MN}^{(J)} = \frac{1}{\sqrt{2J+1}} |M\rangle\langle N| \otimes \mathbf{1}_{\mu_J}. \quad (20)$$

Upon obtaining outcome  $(J, M, N)$ , the data register is left in the (unnormalized) state  $T_{MN}^{(J)} |\psi\rangle$ . This operator selects the component of  $|\psi\rangle$  in the subspace  $\mathcal{W}_N^J$  and maps it into  $\mathcal{W}_M^J$ , leaving the multiplicity degrees of freedom untouched. The outcome occurs with probability

$$p(J, M, N) = \langle \psi | (T_{MN}^{(J)})^\dagger T_{MN}^{(J)} | \psi \rangle = \frac{1}{2J+1} \langle \psi | P_N^J | \psi \rangle, \quad (21)$$

where  $P_N^J = |N\rangle\langle N| \otimes \mathbf{1}_{\mu_J}$  is the projector onto  $\mathcal{W}_N^J$  within the  $J$ -isotypic component. In particular, the probability is independent of  $M$ , so that conditioned on  $J$  and  $N$ , the outcome  $M$  is uniformly distributed over  $\{-J, \dots, J\}$ . For a gauge-invariant input state,  $J = 0$ ,  $M = 0$ , and  $N = 0$  with certainty, and  $T_{00}^{(0)}$  acts as the identity on the singlet sector.

*Step 5. Apply gauge cooling recovery.* If the measurement outcome is  $(J, M, N) = (0, 0, 0)$ , no gauge violation has occurred and no action is taken. Otherwise, we apply a recovery unitary  $R_{J,M}$  to the data register that maps the subspace  $\mathcal{W}_M^J$  into  $\mathcal{W}_0^0$ . Concretely,  $R_{J,M}$  is any unitary on  $\mathcal{H}_v$  satisfying

$$R_{J,M} |M\rangle \otimes |\alpha\rangle = |0\rangle \otimes |\alpha\rangle \quad \alpha = 1, \dots, \min(\mu_J, \mu_0), \quad (22)$$

where  $|M\rangle \otimes |\alpha\rangle$  is understood as a vector in the summand  $V_J \otimes \mathbb{C}^{\mu_J} \subset \mathcal{H}_v$  and  $|0\rangle \otimes |\alpha\rangle$  as a vector in

$V_0 \otimes \mathbb{C}^{\mu_0} \subset \mathcal{H}_v$ , with the action on the remaining basis vectors chosen to complete a unitary. When  $\mu_J > \mu_0$ , the recovery maps only  $\mu_0$  of the  $\mu_J$  multiplicity states back to the singlet sector; the remaining  $\mu_J - \mu_0$  states are mapped to an orthogonal subspace and their information is lost. Note that the recovery depends on  $J$  and  $M$  but not on  $N$ ; the third index records which subspace the state occupied before measurement, but after measurement the data register already resides in  $\mathcal{W}_M^J$  regardless of  $N$ . The full procedure of syndrome extraction (Steps 1–4) followed by conditional recovery constitutes what we refer to as *gauge cooling*. Because the recovery at one vertex modifies the edge spins on the edges incident to that vertex, it can introduce gauge violations at neighboring vertices that share those edges. To account for this, gauge cooling is applied as an iterative sweep; the full cycle of syndrome extraction and recovery is performed at each vertex in sequence, and the sweep is repeated until the gauge-invariant overlap converges. For the single-plaquette geometry studied here, the gauge-violating component decreases geometrically with a contraction factor of approximately 0.45 per sweep, and in the simulations, we use a tolerance-based stopping criterion with a maximum of 10 sweeps.

The gauge cooling procedure returns the state to the singlet sector but does not constitute exact error correction. At vertices where the singlet multiplicity  $\mu_0 > 1$ , the Knill-Laflamme conditions [55] are not satisfied; single-qubit errors on different edges can produce the same gauge syndrome while acting differently on the multiplicity space  $\mathbb{C}^{\mu_0}$ . The recovery therefore eliminates the gauge-variant component of the error but may leave a residual distortion of the logical degrees of freedom within the physical subspace. We show in the supplemental material that, despite this, at any vertex, every single-qubit error is detected by the gauge syndrome, and the residual errors have a bounded Pauli structure on the multiplicity space amenable to further correction by concatenation with a standard stabilizer code.

To validate the protocol, we simulate Trotterized time evolution of the Kogut-Susskind Hamiltonian [29] on a single plaquette with  $j_{\max} = 1/2$  and gauge coupling  $g^2 = 1$ . After each Trotter step, independent noise is applied to every edge, followed by iterative gauge cooling at all four vertices. We compare the fidelity of the corrected state with that of the uncorrected state, measured against the ideal noiseless evolution, under both depolarizing and amplitude damping noise models. The results are shown in Figure 3. Gauge cooling slows the decay of fidelity across all noise rates tested with substantial improvement at later time steps. Details of the Hamiltonian construction, Trotterization, and noise models are provided in the supplemental material. These results establish that active syndrome extraction and recovery can suppress gauge violations and restore approximate gauge invariance in quantum simulations of non-abelian lattice gauge theories on near-term hardware. The extension to larger lattices, where the iterative convergence properties

and the interplay with multiplicity-space errors become more significant, is a natural direction for future work.

- 
- [1] M. K. Gaillard, P. D. Grannis, and F. J. Sciulli, *Reviews of Modern Physics* **71**, S96 (1999).
- [2] D. Tong, *Lecture notes, DAMTP Cambridge* **10**, 74 (2018).
- [3] W. Marciano and H. Pagels, *Physics Reports* **36**, 137 (1978).
- [4] W. Greiner, S. Schramm, and E. Stein, *Quantum chromodynamics* (Springer, 2007).
- [5] J. B. Kogut, *Reviews of Modern Physics* **51**, 659 (1979).
- [6] J. B. Kogut, *Reviews of Modern Physics* **55**, 775 (1983).
- [7] M. Dalmonte and S. Montangero, *Contemporary Physics* **57**, 388 (2016).
- [8] H. J. Rothe, *Lattice gauge theories: an introduction* (World Scientific Publishing Company, 2012).
- [9] K. G. Wilson, *Physical review D* **10**, 2445 (1974).
- [10] S. Durr, Z. Fodor, J. Frison, C. Hoelbling, R. Hoffmann, S. D. Katz, S. Krieg, T. Kurth, L. Lellouch, T. Lippert, *et al.*, *Science* **322**, 1224 (2008).
- [11] S. Borsányi, Z. Fodor, C. Hoelbling, S. D. Katz, S. Krieg, and K. K. Szabo, *Physics Letters B* **730**, 99 (2014).
- [12] A. Bazavov, T. Bhattacharya, C. DeTar, H.-T. Ding, S. Gottlieb, R. Gupta, P. Hegde, U. Heller, F. Karsch, E. Laermann, *et al.*, *Physical Review D* **90**, 094503 (2014).
- [13] Y. Aoki, T. Blum, S. Collins, L. Del Debbio, M. Della Morte, P. Dimopoulos, X. Feng, M. Golterman, S. Gottlieb, R. Gupta, G. Herdoíza, P. Hernandez, A. Jüttner, T. Kaneko, E. Lunghi, S. Meinel, C. Monahan, A. Nicholson, T. Onogi, P. Petreczky, A. Portelli, A. Ramos, S. R. Sharpe, J. N. Simone, S. Sint, R. Sommer, N. Tantalo, R. Van de Water, A. Vaquero, U. Wenger, and H. Wittig (Flavour Lattice Averaging Group (FLAG)), *Phys. Rev. D* **113**, 014508 (2026).
- [14] M. Carmen Bañuls and K. Cichy, *Reports on Progress in Physics* **83**, 024401 (2020).
- [15] J. Berges, S. Borsanyi, D. Sexty, and I.-O. Stamatescu, *Physical Review D—Particles, Fields, Gravitation, and Cosmology* **75**, 045007 (2007).
- [16] H. B. Meyer, *The European Physical Journal A* **47**, 86 (2011).
- [17] M. Troyer and U.-J. Wiese, *Physical review letters* **94**, 170201 (2005).
- [18] I. M. Georgescu, S. Ashhab, and F. Nori, *Reviews of Modern Physics* **86**, 153 (2014).
- [19] A. J. Daley, I. Bloch, C. Kokail, S. Flannigan, N. Pearson, M. Troyer, and P. Zoller, *Nature* **607**, 667 (2022).
- [20] I. Buluta and F. Nori, *Science* **326**, 108 (2009).
- [21] A. Trabesinger, *Nature Physics* **8**, 263 (2012).
- [22] E. Altman, K. R. Brown, G. Carleo, L. D. Carr, E. Demler, C. Chin, B. DeMarco, S. E. Economou, M. A. Eriksen, K.-M. C. Fu, *et al.*, *PRX quantum* **2**, 017003 (2021).
- [23] R. P. Feynman, in *Feynman and computation* (cRc Press, 2018) pp. 133–153.
- [24] S. P. Jordan, K. S. Lee, and J. Preskill, *Science* **336**, 1130 (2012).
- [25] E. A. Martinez, C. A. Muschik, P. Schindler, D. Nigg, A. Erhard, M. Heyl, P. Hauke, M. Dalmonte, T. Monz, P. Zoller, and R. Blatt, *Nature* **534**, 516–519 (2016).
- [26] B. Yang, H. Sun, R. Ott, H.-Y. Wang, T. V. Zache, J. C. Halimeh, Z.-S. Yuan, P. Hauke, and J.-W. Pan, *Nature* **587**, 392 (2020).
- [27] J. Mildenberger, W. Mruczkiewicz, J. C. Halimeh, Z. Jiang, and P. Hauke, *Nature Physics* **21**, 312 (2025).
- [28] E. Zohar, J. I. Cirac, and B. Reznik, *Reports on Progress in Physics* **79**, 014401 (2016).
- [29] J. Kogut and L. Susskind, *Phys. Rev. D* **11**, 395 (1975).
- [30] G. Pardo, T. Greenberg, A. Fortinsky, N. Katz, and E. Zohar, *Phys. Rev. Res.* **5**, 023077 (2023).
- [31] J. Stryker and I. Raychowdhury, *PoS LATTICE2019*, 144 (2020).
- [32] D. B. Kaplan and J. R. Stryker, *Phys. Rev. D* **102**, 094515 (2020).
- [33] J. C. Halimeh and P. Hauke, *Phys. Rev. Lett.* **125**, 030503 (2020).
- [34] J. C. Halimeh, H. Lang, J. Mildenberger, Z. Jiang, and P. Hauke, *PRX Quantum* **2**, 040311 (2021).
- [35] M. Van Damme, H. Lang, P. Hauke, and J. C. Halimeh, *Phys. Rev. B* **107**, 035153 (2023).
- [36] M. C. Tran, Y. Su, D. Carney, and J. M. Taylor, *PRX Quantum* **2**, 010323 (2021).
- [37] J. R. Stryker, *Phys. Rev. A* **99**, 042301 (2019).
- [38] I. Raychowdhury and J. R. Stryker, *Phys. Rev. Res.* **2**, 033039 (2020).
- [39] A. Rajput, A. Roggero, and N. Wiebe, *npj Quantum Inf.* **9**, 41 (2023), arXiv:2112.05186 [quant-ph].
- [40] M. Carena, H. Lamm, Y.-Y. Li, and W. Liu, *Phys. Rev. D* **110**, 054516 (2024).
- [41] N. H. Nguyen, M. C. Tran, Y. Zhu, A. M. Green, C. H. Alderete, Z. Davoudi, and N. M. Linke, *PRX Quantum* **3**, 020324 (2022).
- [42] S. Kühn, J. I. Cirac, and M.-C. Bañuls, *Physical Review A* **90**, 042305 (2014).
- [43] T. V. Zache, F. Hebenstreit, F. Jendrzejewski, M. K. Oberthaler, J. Berges, and P. Hauke, *Quantum science and technology* **3**, 034010 (2018).
- [44] N. Klco, E. F. Dumitrescu, A. J. McCaskey, T. D. Morris, R. C. Pooser, M. Sanz, E. Solano, P. Lougovski, and M. J. Savage, *Physical Review A* **98**, 032331 (2018).
- [45] D. Gottesman, *Stabilizer codes and quantum error correction* (California Institute of Technology, 1997).
- [46] Z. P. Bradshaw, J. J. Dale, and E. N. Evans, *Annals of Physics* **487**, 170353 (2026).
- [47] Z. P. Bradshaw, M. L. LaBorde, and D. Montero, *Phys. Rev. A* , (2026).
- [48] J. Diestel and A. Spalsbury, *The joys of Haar measure* (American Mathematical Soc., 2014).
- [49] A. A. Mele, *Quantum* **8**, 1340 (2024).
- [50] M. L. LaBorde, S. Rethinasamy, and M. M. Wilde, *Quantum* **7**, 1120 (2023).
- [51] Z. P. Bradshaw, M. L. LaBorde, and M. M. Wilde, *Proceedings of the Royal Society A: Mathematical, Physical and Engineering Sciences* **479**, 10.1098/rspa.2022.0733 (2023).
- [52] M. L. LaBorde, S. Rethinasamy, and M. M. Wilde, *Quantum algorithms for realizing symmetric, asymmetric, and antisymmetric projectors* (2024), arXiv:2407.17563

- [quant-ph].
- [53] H. Lamm, S. Lawrence, and Y. Yamauchi, arXiv preprint arXiv:2005.12688 (2020).
  - [54] E. Knill, *Nature* **434**, 39 (2005).
  - [55] E. Knill and R. Laflamme, *Physical Review A* **55**, 900 (1997).
  - [56] C. Dankert, R. Cleve, J. Emerson, and E. Livine, *Physical Review A* **80**, 10.1103/physreva.80.012304 (2009).
  - [57] D. C. McKay, I. Hincks, E. J. Pritchett, M. Carroll, L. C. Govia, and S. T. Merkel, arXiv preprint arXiv:2311.05933 (2023).
  - [58] J. E. Mandula and M. Ogilvie, *Physics Letters B* **185**, 127 (1987).
  - [59] A. Cucchieri and T. Mendes, *Computer physics communications* **154**, 1 (2003).

## I. PETER-WEYL DECOMPOSITION AND VERTEX REGROUPING

In this section, we provide the details of the passage from the Peter-Weyl decomposition on individual edges to the Clebsch-Gordan decomposition at each vertex, which was summarized in the main text.

By the Peter-Weyl theorem, each link Hilbert space  $\mathcal{H}_e = L^2(\text{SU}(2))$  decomposes as

$$\mathcal{H}_e \cong \bigoplus_{j \in \frac{1}{2}\mathbb{N}_0} V_j \otimes V_j^*, \quad (\text{S1})$$

where  $V_j$  is the carrier space of the spin- $j$  irrep  $\pi_j$  with dimension  $d_j = 2j + 1$ . The full Hilbert space of the lattice (restricting to gauge degrees of freedom) is the tensor product over all edges,

$$\bigotimes_{e \in E} \mathcal{H}_e = \bigotimes_{e \in E} \bigoplus_{j \in \frac{1}{2}\mathbb{N}_0} V_j \otimes V_j^*. \quad (\text{S2})$$

Distributing the tensor product over the direct sums, this becomes

$$\bigoplus_{\{j_e\}_{e \in E}} \bigotimes_{e \in E} (V_{j_e} \otimes V_{j_e}^*), \quad (\text{S3})$$

where the direct sum runs over all assignments of a spin label  $j_e \in \frac{1}{2}\mathbb{N}_0$  to each edge of the lattice. Each summand is a tensor product of finite-dimensional spaces labeled by a fixed configuration of edge spins.

We now regroup the factors in each summand by vertex rather than by edge. Recall that an oriented edge  $e$  with source vertex  $s(e)$  and target vertex  $t(e)$  contributes a factor of  $V_{j_e}$  that transforms under gauge transformations at  $s(e)$  and a factor of  $V_{j_e}^*$  that transforms at  $t(e)$ . This follows from the definition of the gauge action: a gauge transformation  $h_v$  at vertex  $v$  acts via the left regular representation on outgoing edges (affecting the  $m$  index of  $V_{j_e}$ ) and via the right regular representation on incoming edges (affecting the  $n$  index of  $V_{j_e}^*$ ).

Collecting all factors associated with a given vertex  $v$ , we define the vertex Hilbert space

$$\mathcal{H}_v(\{j_e\}) = \bigotimes_{\substack{e \in E \\ s(e)=v}} V_{j_e} \otimes \bigotimes_{\substack{e \in E \\ t(e)=v}} V_{j_e}^*. \quad (\text{S4})$$

For a fixed assignment of edge spins, the full Hilbert space then factorizes over vertices:

$$\bigotimes_{e \in E} (V_{j_e} \otimes V_{j_e}^*) \cong \bigotimes_{v \in V} \mathcal{H}_v(\{j_e\}). \quad (\text{S5})$$

This factorization is possible because each edge contributes exactly one tensor factor ( $V_{j_e}$ ) to its source vertex and one factor ( $V_{j_e}^*$ ) to its target vertex, and every factor is thereby assigned to exactly one vertex.

At each vertex  $v$ , the space  $\mathcal{H}_v(\{j_e\})$  is a tensor product of  $\text{SU}(2)$  irreps (both fundamental and contragredient). Since  $V_j^* \cong V_j$  for  $\text{SU}(2)$  (the equivalence being implemented by the antisymmetric tensor  $\epsilon_{mm'}$  =

$(-1)^{j-m}\delta_{m,-m'}$ ), the vertex Hilbert space is equivalent to a tensor product of standard  $\text{SU}(2)$  representations. The Clebsch-Gordan decomposition then gives

$$\mathcal{H}_v(\{j_e\}) \cong \bigoplus_{J_v} V_{J_v} \otimes \mathbb{C}^{\mu_{J_v}}, \quad (\text{S6})$$

where  $J_v$  labels the total angular momentum at vertex  $v$  and  $\mu_{J_v}$  is the multiplicity of the spin- $J_v$  irrep in the decomposition. The gauge transformation  $U^{(v)}(h)$  acts as  $\pi_{J_v}(h) \otimes \mathbf{1}_{\mu_{J_v}}$  within each summand, so the Gauss law constraint  $U^{(v)}(h) = \mathbf{1}$  for all  $h$  selects the  $J_v = 0$  (singlet) sector. The physical subspace at vertex  $v$  is therefore  $V_0 \otimes \mathbb{C}^{\mu_0} \cong \mathbb{C}^{\mu_0}$ , and the physical degrees of freedom reside entirely in the multiplicity space.

The multiplicity  $\mu_0$  depends on both the number of edges meeting at  $v$  and the spin labels assigned to those edges. For coordination-2 vertices (as in the single-plaquette geometry), the coupling of two spin-1/2 representations gives  $\mu_0 = 1$  for each edge-spin assignment that admits a singlet. For coordination-4 vertices (as in the square lattice), the coupling  $(1/2)^{\otimes 4}$  yields  $\mu_0 = 2$ , so the physical subspace at each vertex carries a nontrivial two-dimensional multiplicity space. This distinction is central to the error correction analysis in Section VIII.

## II. GROUP ALGEBRA BASIS AND WIGNER BASIS

In this section, we clarify the relationship between the two bases that appear in the syndrome extraction protocol: the group algebra basis  $\{|g\rangle\}$  used in Steps 1–2 and the Wigner basis  $\{|j, m, n\rangle\}$  used in the measurement of Step 4.

A state  $\psi \in L^2(\text{SU}(2))$  is a square-integrable function  $\psi : \text{SU}(2) \rightarrow \mathbb{C}$ . The Peter-Weyl theorem provides a complete orthonormal basis for this space in terms of the normalized Wigner matrix elements  $\sqrt{2j+1}[\pi_j(g)]_{mn}$ , so that any state can be expanded as

$$\psi(g) = \sum_j \sqrt{2j+1} \sum_{m,n=-j}^j \hat{\psi}_{mn}^{(j)} D_{mn}^{(j)}(g), \quad (\text{S7})$$

where the Peter-Weyl coefficients are given by

$$\hat{\psi}_{mn}^{(j)} = \sqrt{2j+1} \int_{\text{SU}(2)} \psi(g) \overline{D_{mn}^{(j)}(g)} dg. \quad (\text{S8})$$

The group quantum Fourier transform  $\text{QFT}_{\text{SU}(2)}$  is the unitary change of basis from the group element picture to the representation picture. It takes a state described by its values  $\psi(g)$  and re-expresses it in terms of its Peter-Weyl coefficients  $\hat{\psi}_{mn}^{(j)}$ .

The group element  $|g\rangle$  is not a state in  $L^2(\text{SU}(2))$  but rather a distributional object satisfying  $\langle g|g'\rangle = \delta(g, g')$  with respect to the Haar measure, analogous to the position eigenstate  $|x\rangle$  in ordinary quantum mechanics. The

value of a state at a group element is recovered via  $\psi(g) = \langle g|\psi\rangle$ , exactly as  $\psi(x) = \langle x|\psi\rangle$  in the position representation.

The analogy with ordinary quantum mechanics is precise and illuminating:

Quantum mechanics	Gauge theory
Position basis $ x\rangle$	Group element basis $ g\rangle$
Momentum basis $ p\rangle$	Wigner basis $ j, m, n\rangle$
Fourier transform	QFT <sub>SU(2)</sub>
$ p=0\rangle = \int  x\rangle dx$	$ 0, 0, 0\rangle = \int  g\rangle dg$

A uniform superposition over all group elements corresponds to a function that is constant on SU(2). Its Peter-Weyl expansion has support only on  $j=0$ , since the constant function is precisely the trivial representation. In the Wigner basis, this state is  $|j=0, m=0, n=0\rangle$ . This is the non-abelian analogue of the fact that a uniform superposition over all position states corresponds to the definite zero-momentum state  $|p=0\rangle$ .

In the syndrome extraction circuit, this duality is exploited as follows. The preparation  $F_G$  creates a uniform superposition over group elements (or, in the truncated setting, over a  $t$ -design), expressing the  $J_v=0$  state in the group algebra basis. This basis is chosen because the controlled gauge action  $\sum_i |g_i\rangle\langle g_i| \otimes U^{(v)}(g_i)$  is diagonal in the group element basis, making the controlled operation straightforward to implement. The QFT<sub>SU(2)</sub> then transforms the ancilla to the Wigner basis, where the measurement in  $\{|j, m, n\rangle\}$  extracts the syndrome  $(J, M, N)$ . The circuit thus never works in a single basis throughout; it uses the group algebra basis where the controlled- $U$  is natural and the Wigner basis where the measurement is natural, with the group QFT serving as the bridge between the two.

A note on the status of the basis states appearing in the circuit is in order. The group element states  $|g\rangle$  discussed above are distributional objects, not normalizable vectors, exactly as the position eigenstates  $|x\rangle$  are not elements of  $L^2(\mathbb{R})$ . The syndrome extraction circuit, however, operates on a finite-dimensional ancilla register  $\mathbb{C}^{n_t}$  whose computational basis vectors  $\{|g_1\rangle, \dots, |g_{n_t}\rangle\}$  are labeled by the elements of a unitary  $t$ -design. These are proper orthonormal states satisfying  $\langle g_i|g_k\rangle = \delta_{ik}$ , related to the distributional picture in the same way that a finite lattice of position eigenstates relates to the continuum  $|x\rangle$  basis. The controlled gauge action  $\sum_i |g_i\rangle\langle g_i| \otimes U^{(v)}(g_i)$  and the truncated group QFT are both finite-dimensional operators on this register. The  $t$ -design condition derived in Section III guarantees that this discretization introduces no error in the syndrome extraction for edge Hilbert spaces truncated at  $j_{\max}$ , so the formal expressions involving the Haar measure and the continuum QFT serve as the mathematical ideal of which the circuit is an exact finite-dimensional realization within the truncated theory.

### III. $t$ -DESIGN APPROXIMATION

The syndrome extraction protocol calls for a uniform superposition over SU(2), which is an infinite-dimensional object. On finite-dimensional quantum hardware, this must be replaced by a finite approximation. In this section, we show that a uniform superposition over a unitary  $t$ -design provides a controlled approximation, and we determine the required design strength as a function of the truncation cutoff  $j_{\text{cut}}$ .

A unitary  $t$ -design on SU(2) is a finite set  $\{g_1, \dots, g_{n_t}\} \subset \text{SU}(2)$  such that the uniform average over the set reproduces the Haar integral for all polynomials in the matrix entries of  $g$  and  $\bar{g}$  of degree at most  $t$  in each [49, 56]. Formally,

$$\frac{1}{n_t} \sum_{i=1}^{n_t} f(g_i) = \int_{\text{SU}(2)} f(g) dg \quad (\text{S9})$$

for every polynomial  $f$  of degree at most  $t$  in the matrix entries of  $g$  and degree at most  $t$  in the entries of  $\bar{g}$ .

The key operator in the syndrome extraction is  $T_{MN}^{(J)}$  defined in Eq. (18) of the main text,

$$T_{MN}^{(J)} = \frac{\sqrt{2J+1}}{n_t} \sum_{i=1}^{n_t} [\overline{\pi_J(g_i)}]_{MN} U^{(v)}(g_i). \quad (\text{S10})$$

This is the discrete approximation to the Haar integral

$$\sqrt{2J+1} \int_{\text{SU}(2)} \overline{D_{MN}^{(J)}(g)} U^{(v)}(g) dg. \quad (\text{S11})$$

To evaluate when the discrete sum equals the integral exactly, we must determine the polynomial bidegree of the integrand in the matrix entries of  $g$  and  $\bar{g}$  separately, since the  $t$ -design condition (S9) imposes independent degree constraints on each.

The factor  $\overline{D_{MN}^{(J)}(g)}$  is the complex conjugate of a spin- $J$  representation matrix element. Since  $D_{MN}^{(J)}(g) = [\pi_J(g)]_{MN}$  is a polynomial of degree  $2J$  in the matrix entries of  $g$  (and degree 0 in the entries of  $\bar{g}$ ), its complex conjugate  $\overline{D_{MN}^{(J)}(g)}$  is a polynomial of degree 0 in  $g$  and degree  $2J$  in  $\bar{g}$ .

The gauge action  $U^{(v)}(g)$  acts on the edges incident to vertex  $v$ , but the polynomial type of each edge contribution depends on the orientation. On an outgoing edge (where  $v$  is the source), the gauge transformation acts via the left regular representation  $L_g$ , whose matrix elements on the spin- $j_e$  sector are  $[\pi_{j_e}(g)]_{m'm}$ . This follows from  $L_g f(h) = f(g^{-1}h)$  together with the unitarity of  $\pi_{j_e}$ , which gives  $[\pi_{j_e}(g^{-1})]_{mm'} = [\pi_{j_e}(g)^\dagger]_{mm'} = [\overline{\pi_{j_e}(g)}]_{m'm}$ . Each such factor is a polynomial of degree 0 in  $g$  and degree  $2j_e$  in  $\bar{g}$ . On an incoming edge (where  $v$  is the target), the gauge transformation acts via the right regular representation  $R_g$ , whose matrix elements are  $[\pi_{j_e}(g)]_{n'n}$ , a polynomial of degree  $2j_e$  in  $g$  and degree 0 in  $\bar{g}$ .

The matrix element of the full integrand between any two basis states is therefore a polynomial with bidegree

$$\deg_g = 2 \sum_{e=t(v)} j_e, \quad \deg_{\bar{g}} = 2J + 2 \sum_{e=s(v)} j_e. \quad (\text{S12})$$

The  $t$ -design condition (S9) guarantees exact integration provided

$$t \geq \max\left(2 \sum_{e \in \text{in}(v)} j_e, 2J + 2 \sum_{e \in \text{out}(v)} j_e\right), \quad (\text{S13})$$

where  $\text{in}(v)$  and  $\text{out}(v)$  denote the sets of incoming and outgoing edges at  $v$ , respectively.

Since the truncation restricts  $J \leq j_{\text{cut}}$ , each edge spin satisfies  $j_e \leq j_{\text{max}}$ , and the maximum total angular momentum at a vertex with  $k$  incident edges is  $J_{\text{max}} = k \cdot j_{\text{max}}$ , a sufficient condition is

$$t \geq 2k \cdot j_{\text{max}} + 2k_{\text{out}} \cdot j_{\text{max}}, \quad (\text{S14})$$

where  $k_{\text{out}}$  is the number of outgoing edges at the vertex. For the single-plaquette geometry ( $k = 2$ ,  $k_{\text{out}} = 1$ ,  $j_{\text{max}} = 1/2$ ), this gives  $t \geq 3$ . For a square lattice vertex ( $k = 4$ ,  $k_{\text{out}} = 2$ ,  $j_{\text{max}} = 1/2$ ), the requirement is  $t \geq 6$ .

When the  $t$ -design condition is satisfied, the discrete operator  $T_{MN}^{(J)}$  equals the continuum operator exactly, and the syndrome extraction is faithful. The size  $n_t$  of the  $t$ -design determines the dimension of the ancilla register; a  $t$ -design on  $\text{SU}(2)$  requires at least  $\sum_{j=0}^t (2j+1)^2 = O(t^3)$  elements (by dimension counting of the Peter-Weyl basis up to spin  $t$ ), so the ancilla overhead grows polynomially with the coordination number and  $j_{\text{max}}$ .

#### IV. TRUNCATION OF THE GROUP QFT

The group quantum Fourier transform  $\text{QFT}_{\text{SU}(2)}$  as defined in Eq. (15) of the main text acts on an infinite-dimensional Hilbert space, since the Peter-Weyl decomposition of  $L^2(\text{SU}(2))$  involves all spins  $j \in \frac{1}{2}\mathbb{N}_0$ . In this section we justify the truncation to  $j \leq j_{\text{cut}}$  and characterize the resulting map.

The truncated QFT is defined by

$$\text{QFT}_{\text{SU}(2)}^{\leq j_{\text{cut}}} |g\rangle = \sum_{j=0}^{j_{\text{cut}}} \sqrt{\frac{2j+1}{n_t}} \sum_{m,n=-j}^j [\pi_j(g)]_{mn} |j, m, n\rangle, \quad (\text{S15})$$

where  $j$  ranges over half-integer steps. The output space is spanned by  $\{|j, m, n\rangle : j \leq j_{\text{cut}}, -j \leq m, n \leq j\}$  and has dimension

$$d_{\text{out}} = \sum_{j=0}^{j_{\text{cut}}} (2j+1)^2. \quad (\text{S16})$$

For  $j_{\text{cut}} = 1/2$ , this gives  $d_{\text{out}} = 1 + 4 = 5$ .

The input space is the  $n_t$ -dimensional ancilla register spanned by  $\{|g_1\rangle, \dots, |g_{n_t}\rangle\}$ . For the truncated map to

be well defined, we need  $n_t \geq d_{\text{out}}$ . When  $n_t > d_{\text{out}}$ , the map has a nontrivial kernel; when  $n_t = d_{\text{out}}$ , it is a square matrix and can be unitary if the  $t$ -design elements are chosen appropriately.

#### A. Isometry property

The truncated QFT acts as an isometry from the ancilla register into the output subspace on all states within the truncated edge Hilbert space, provided the  $t$ -design condition from Section III is satisfied. To see this, consider the inner product of two output states:

$$\begin{aligned} & \langle g_i | (\text{QFT}^{\leq j_{\text{cut}}})^\dagger \text{QFT}^{\leq j_{\text{cut}}} |g_k\rangle \\ &= \sum_{j=0}^{j_{\text{cut}}} \frac{2j+1}{n_t} \sum_{m,n} [\pi_j(g_i)]_{mn} [\overline{\pi_j(g_k)}]_{mn} \\ &= \sum_{j=0}^{j_{\text{cut}}} \frac{2j+1}{n_t} \chi_j(g_i g_k^{-1}), \end{aligned} \quad (\text{S17})$$

where  $\chi_j(g) = \text{Tr}[\pi_j(g)]$  is the character of the spin- $j$  representation. In the continuum ( $j_{\text{cut}} \rightarrow \infty$ ), the Peter-Weyl completeness relation gives  $\sum_j (2j+1) \chi_j(g_i g_k^{-1}) = \delta(g_i, g_k)$ , recovering the orthonormality of the distributional states  $\langle g|g'\rangle = \delta(g, g')$ . On the discrete ancilla register, the  $t$ -design condition replaces the Haar integral with a finite sum, introducing a factor of  $n_t$  that is absorbed by the  $1/\sqrt{n_t}$  prefactor in the truncated QFT.

The key observation is that the syndrome extraction does not require the full delta function. The operator  $T_{MN}^{(J)}$  acts within the  $J$ -isotypic component of  $\mathcal{H}_v$ , and the vertex Hilbert space is itself truncated to  $j_e \leq j_{\text{max}}$  on each edge. The Clebsch-Gordan decomposition at a vertex with  $k$  edges carrying spins at most  $j_{\text{max}}$  produces total angular momenta  $J_v \leq k \cdot j_{\text{max}}$ . Therefore, the syndrome extraction is exact provided

$$j_{\text{cut}} \geq k \cdot j_{\text{max}}, \quad (\text{S18})$$

which ensures that all gauge-violation sectors that can arise from the truncated edge Hilbert spaces are resolved by the measurement. For the single-plaquette geometry ( $k = 2$ ,  $j_{\text{max}} = 1/2$ ), this gives  $j_{\text{cut}} \geq 1$ , so the truncated QFT with  $j_{\text{cut}} = 1$  is sufficient.

#### B. Embedding into a unitary

When  $n_t > d_{\text{out}}$ , the truncated QFT is a rectangular matrix of size  $d_{\text{out}} \times n_t$ . To implement it as a quantum circuit, we embed it into a unitary on the full  $n_t$ -dimensional ancilla register. Let  $W$  denote the  $d_{\text{out}} \times n_t$  matrix of the truncated QFT. Since  $W$  is an isometry ( $WW^\dagger = \mathbf{1}_{d_{\text{out}}}$  up to the truncation corrections discussed above), we can extend it to a unitary  $\tilde{W}$  of size  $n_t \times n_t$  by appending

$n_t - d_{\text{out}}$  orthonormal rows that span the orthogonal complement of the range of  $W$ . The choice of these additional rows does not affect the syndrome extraction, since measurement outcomes in the  $|j, m, n\rangle$  basis with  $j \leq j_{\text{cut}}$  are determined entirely by  $W$ , and outcomes corresponding to the orthogonal complement indicate that the ancilla has landed outside the truncated Wigner basis. Such outcomes can be treated as a “no information” result, after which no recovery is applied. For the parameter regime used in this work ( $j_{\text{cut}} \geq k \cdot j_{\text{max}}$ ), such outcomes have exactly zero probability.

### C. Effect on syndrome extraction

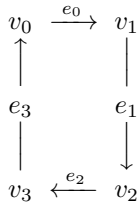
When the truncation condition  $j_{\text{cut}} \geq k \cdot j_{\text{max}}$  is satisfied, the syndrome operators  $T_{MN}^{(J)}$  for all  $J$  appearing in the Clebsch-Gordan decomposition of the vertex Hilbert space are computed exactly. The truncation then has no effect on the syndrome extraction or on the subsequent recovery.

When  $j_{\text{cut}} < k \cdot j_{\text{max}}$ , some high- $J$  gauge-violation sectors are not resolved by the measurement. Errors that map the state into these unresolved sectors will not be detected. For the single-plaquette geometry with  $j_{\text{max}} = 1/2$ , the maximum total angular momentum at a coordination-2 vertex is  $J_{\text{max}} = 1$ , so the choice  $j_{\text{cut}} = 1$  resolves all sectors and no information is lost.

## V. SINGLE-PLAQUETTE LATTICE GEOMETRY

### A. Geometry and edge orientations

The numerical demonstration in the main text uses a single plaquette consisting of four vertices  $\{v_0, v_1, v_2, v_3\}$  and four oriented edges  $\{e_0, e_1, e_2, e_3\}$  arranged as follows:



The edge orientations are chosen so that the plaquette operator traces clockwise around the square:  $e_0 : v_0 \rightarrow v_1$ ,  $e_1 : v_1 \rightarrow v_2$ ,  $e_2 : v_2 \rightarrow v_3$ ,  $e_3 : v_3 \rightarrow v_0$ . Each vertex has coordination number 2, with one outgoing and one incoming edge:

Vertex	Outgoing	Incoming
$v_0$	$e_0$	$e_3$
$v_1$	$e_1$	$e_0$
$v_2$	$e_2$	$e_1$
$v_3$	$e_3$	$e_2$

With the truncation  $j_{\text{max}} = 1/2$ , each edge carries a 5-dimensional Hilbert space spanned by the Wigner basis states  $\{|j, m, n\rangle\}$ :

Index	$ j, m, n\rangle$
0	$ 0, 0, 0\rangle$
1	$ \frac{1}{2}, -\frac{1}{2}, -\frac{1}{2}\rangle$
2	$ \frac{1}{2}, -\frac{1}{2}, +\frac{1}{2}\rangle$
3	$ \frac{1}{2}, +\frac{1}{2}, -\frac{1}{2}\rangle$
4	$ \frac{1}{2}, +\frac{1}{2}, +\frac{1}{2}\rangle$

The total Hilbert space dimension is  $5^4 = 625$ . Throughout this work, we treat each edge as a  $d$ -dimensional qudit ( $d = 5$  for  $j_{\text{max}} = 1/2$ ) for notational clarity; in practice, each edge can be encoded into  $\lceil \log_2 d \rceil = 3$  qubits by embedding the  $d$ -dimensional Hilbert space into a subspace of the  $2^3$ -dimensional register.

### B. Kogut-Susskind Hamiltonian

The Kogut-Susskind Hamiltonian [29] for pure SU(2) gauge theory on this plaquette is  $H = H_E + H_B$ , where  $H_E$  is the electric (kinetic) term and  $H_B$  is the magnetic (plaquette) term.

#### 1. Electric term

The electric Hamiltonian is

$$H_E = \frac{g^2}{2} \sum_{e \in E} \hat{j}_e (\hat{j}_e + 1), \quad (\text{S19})$$

where  $\hat{j}_e$  is the Casimir operator on edge  $e$ , diagonal in the Wigner basis with eigenvalue  $j_e(j_e + 1)$ . For  $j_{\text{max}} = 1/2$ , the single-edge electric Hamiltonian is

$$H_E^{(e)} = \frac{g^2}{2} \text{diag}(0, \frac{3}{4}, \frac{3}{4}, \frac{3}{4}, \frac{3}{4}), \quad (\text{S20})$$

where the entries correspond to  $j = 0$  (eigenvalue 0) and the four  $j = 1/2$  states (eigenvalue  $3/4$ ). The full electric Hamiltonian is  $H_E = \sum_{e=0}^3 H_E^{(e)} \otimes \mathbf{1}_{\bar{e}}$ , where  $\mathbf{1}_{\bar{e}}$  denotes the identity on all edges other than  $e$ . Since  $H_E$  is diagonal in the Wigner basis, the unitary  $e^{-iH_E dt}$  is trivially computed as a diagonal matrix.

#### 2. Magnetic (plaquette) term

The magnetic Hamiltonian involves the trace of the product of link operators around the plaquette:

$$H_B = -\frac{1}{g^2} \text{Re}(\text{Tr}_{1/2}[U_{\text{plaq}}]), \quad (\text{S21})$$

where  $\text{Tr}_{1/2}$  denotes the trace in the fundamental ( $j = 1/2$ ) representation and

$$U_{\text{plaq}} = U_{e_0} U_{e_1} U_{e_2} U_{e_3} \quad (\text{S22})$$

is the ordered product of link operators around the plaquette. In the group element picture, the plaquette trace is  $\text{Tr}(g_0 g_1 g_2 g_3)$  where  $g_e$  is the  $\text{SU}(2)$  element on edge  $e$ .

To compute the matrix elements of  $H_B$  in the Wigner basis, we use the identity for the integral of a product of three Wigner  $D$ -functions over  $\text{SU}(2)$ :

$$\int_{\text{SU}(2)} \overline{D_{m'n'}^{(j')}(g)} D_{ab}^{(1/2)}(g) D_{mn}^{(j)}(g) dg = \frac{C_{\frac{1}{2}a, jm}^{j'm'} C_{\frac{1}{2}b, jn}^{j'n'}}{2j'+1}, \quad (\text{S23})$$

where  $C_{j_1 m_1, j_2 m_2}^{j_3 M}$  denotes the Clebsch-Gordan coefficient  $\langle j_1, m_1; j_2, m_2 | J, M \rangle$ . This integral arises because each edge contributes one  $D$ -function from the bra, one from the fundamental-representation link operator, and one from the ket.

For each edge, we define the tensor

$$T_{ab, I'I}^{(e)} = \sqrt{d_{j'} d_j} \frac{C_{\frac{1}{2}a, jm}^{j'm'} C_{\frac{1}{2}b, jn}^{j'n'}}{d_{j'}}, \quad (\text{S24})$$

where  $I = (j, m, n)$  and  $I' = (j', m', n')$  are compound indices labeling the single-edge Wigner basis,  $a$  and  $b$  are fundamental-representation indices contracted around the plaquette, and the factors of  $\sqrt{d_j}$  arise from the normalization of the Wigner basis. The selection rules enforce  $m' = a + m$ ,  $n' = b + n$ , and  $|j - 1/2| \leq j' \leq j + 1/2$ .

The matrix element of the plaquette trace in the full Wigner basis is then

$$\begin{aligned} & \langle I'_0 I'_1 I'_2 I'_3 | \text{Tr}_{1/2}(U_{\text{plaq}}) | I_0 I_1 I_2 I_3 \rangle \\ &= \sum_{a, b_0, b_1, b_2} T_{a b_0, I'_0 I_0}^{(e_0)} T_{b_0 b_1, I'_1 I_1}^{(e_1)} \\ & \quad \times T_{b_1 b_2, I'_2 I_2}^{(e_2)} T_{b_2 a, I'_3 I_3}^{(e_3)}, \end{aligned} \quad (\text{S25})$$

where the sum runs over all fundamental-representation indices. The cyclic contraction of the indices  $a, b_0, b_1, b_2$  reflects the trace structure of the plaquette. The full magnetic Hamiltonian is obtained by taking the real part and multiplying by  $-1/g^2$ .

We have verified numerically that the resulting  $625 \times 625$  matrix  $H_B$  is Hermitian, that  $[H_B, C^{(v)}] = 0$  for the gauge Casimir  $C^{(v)}$  at each vertex (confirming gauge invariance), and that it agrees with an independent Monte Carlo evaluation of the Haar integral to within statistical precision. For the simulations, we use coupling  $g^2 = 1$ .

### C. Clebsch-Gordan decomposition at coordination-2 vertices

At each vertex of the single plaquette, the gauge transformation  $U^{(v)}(h)$  acts on two indices: the  $m$  index of the

outgoing edge (via the left regular representation) and the  $n$  index of the incoming edge (via the right regular representation). The vertex Hilbert space for fixed edge spins  $j_{\text{out}}$  and  $j_{\text{in}}$  is therefore  $V_{j_{\text{out}}} \otimes V_{j_{\text{in}}}^*$ . Since  $V_j^* \cong V_j$  for  $\text{SU}(2)$ , this is equivalent to coupling two angular momenta.

For  $j_{\text{max}} = 1/2$ , the possible combinations and their Clebsch-Gordan decompositions are:

$j_{\text{out}}$	$j_{\text{in}}$	Decomposition
0	0	$J = 0$ ( $\mu_0 = 1$ )
0	1/2	$J = 1/2$ ( $\mu_{1/2} = 1$ )
1/2	0	$J = 1/2$ ( $\mu_{1/2} = 1$ )
1/2	1/2	$J = 0 \oplus J = 1$ ( $\mu_0 = 1, \mu_1 = 1$ )

The singlet ( $J = 0$ ) sector appears in the first and fourth rows, each with multiplicity  $\mu_0 = 1$ . These live in different edge-spin blocks that are not mixed by gauge transformations. Within each block,  $\mu_0 = 1$ .

The vertex Hilbert space  $\mathcal{H}_v$  collects only the indices that transform under the gauge action at  $v$ :  $V_{j_{\text{out}}}$  from the outgoing edge and  $V_{j_{\text{in}}}^*$  from the incoming edge. Summing over all edge-spin assignments, the total dimension is  $1 + 2 + 2 + 4 = 9$ . The  $J$  sectors across this 9-dimensional space are:  $J = 0$  with total multiplicity 2 (one singlet from each of the  $(0, 0)$  and  $(1/2, 1/2)$  blocks),  $J = 1/2$  with total multiplicity 2 (one copy from each of the  $(0, 1/2)$  and  $(1/2, 0)$  blocks, each carrying  $2J + 1 = 2$  states), and  $J = 1$  with multiplicity 1 (from the  $(1/2, 1/2)$  block, carrying  $2J + 1 = 3$  states). This accounts for all  $2 + 4 + 3 = 9$  states.

In practice, the CG basis is constructed numerically by building the gauge generators  $G_a^{(v)}$  ( $a = x, y, z$ ) at each vertex, forming the Casimir operator  $C^{(v)} = \sum_a (G_a^{(v)})^2$ , and diagonalizing  $C^{(v)}$  and  $G_z^{(v)}$  simultaneously. The eigenvalues of  $C^{(v)}$  are  $J(J + 1)$ , giving the  $J$  quantum number, and the eigenvalues of  $G_z^{(v)}$  within each  $J$  sector give  $M$ .

The gauge generators act on the 5-dimensional edge space as follows. On the outgoing edge, the generator of left multiplication  $L_a$  acts on the  $m$  index within each  $(j, n)$  block:

$$L_a |j, m, n\rangle = \sum_{m'} [\mathcal{J}_a^{(j)}]_{m'm} |j, m', n\rangle, \quad (\text{S26})$$

where  $\mathcal{J}_a^{(j)}$  is the spin- $j$  representation of the  $\mathfrak{su}(2)$  generator  $J_a$ . Note that because  $L_h f(g) = f(h^{-1}g)$ , the generators of  $L$  carry a sign relative to the representation matrices:  $\mathcal{J}_a^{(L)} = -J_a^*$ . On the incoming edge, the generator of right multiplication  $R_a$  acts on the  $n$  index:

$$R_a |j, m, n\rangle = \sum_{n'} [\mathcal{J}_a^{(j)}]_{n'n} |j, m, n'\rangle. \quad (\text{S27})$$

The full gauge generator at vertex  $v$  is  $G_a^{(v)} = L_a^{(e_{\text{out}})} \otimes \mathbf{1}_{e_{\text{in}}} + \mathbf{1}_{e_{\text{out}}} \otimes R_a^{(e_{\text{in}})}$ , embedded into the full 625-dimensional space by tensoring with the identity on the remaining two edges.

## D. Recovery operator construction

The gauge cooling recovery operator  $R_{J,M}$  maps the subspace  $\mathcal{W}_M^J$  back to  $\mathcal{W}_0^0$  at each vertex. For the single-plaquette geometry where  $\mu_0 = 1$  within each edge-spin block, the recovery is uniquely determined up to a phase: it maps the single basis vector in  $\mathcal{W}_M^J$  (for a given edge-spin assignment) to the single singlet state in  $\mathcal{W}_0^0$ .

The construction proceeds as follows. Having obtained the CG basis by diagonalizing the Casimir and  $G_z$  as described above, we organize the basis vectors by  $J$  sector. Within each  $J$  sector, the  $M$  values range from  $-J$  to  $J$ , and we need the basis vectors at different  $M$  values to be consistently related by the gauge raising and lowering operators. This ensures that the recovery operator preserves the multiplicity structure.

Starting from the lowest-weight states ( $M = -J$ ) within each  $J$  sector, we apply the raising operator  $G_+ = G_x + iG_y$  to generate all higher- $M$  states:

$$|J, M + 1, \alpha\rangle = \frac{G_+ |J, M, \alpha\rangle}{\sqrt{J(J+1) - M(M+1)}}, \quad (\text{S28})$$

where  $\alpha$  labels the multiplicity. This produces a consistently labeled basis  $\{|J, M, \alpha\rangle\}$  in which states at different  $M$  with the same  $\alpha$  are related by the standard angular momentum algebra.

The Kraus operators for the gauge cooling channel are then

$$K_{J,N} = \sum_{\alpha=1}^{\min(\mu_J, \mu_0)} |0, 0, \alpha\rangle \langle J, N, \alpha|, \quad (\text{S29})$$

where the sum runs over the multiplicity index. This operator maps states in  $\mathcal{W}_N^J$  to  $\mathcal{W}_0^0$ , preserving the multiplicity label. As shown in Step 4 of the main text, the measurement outcome  $(J, M, N)$  produces the same Kraus operator  $K_{J,N}$  for all values of  $M$  (the  $M$  dependence cancels because  $R_{J,M}$  undoes the  $M$ -shift introduced by  $T_{MN}^{(J)}$ ). The full gauge cooling channel at a single vertex is therefore

$$\mathcal{E}(\rho) = \sum_{J,N} K_{J,N} \rho K_{J,N}^\dagger, \quad (\text{S30})$$

which is trace-preserving:  $\sum_{J,N} K_{J,N}^\dagger K_{J,N} = \sum_{J,N} P_N^J = \mathbf{1}$ .

In practice, the recovery can be further refined by matching each non-singlet state  $|J, N, \alpha\rangle$  to the singlet state  $|0, 0, \alpha'\rangle$  that shares the same spectator quantum numbers (the edge-spin labels and indices not acted on by the gauge transformation at  $v$ ). This spectator-preserving assignment minimizes changes to the edge states, reducing disruption to neighboring vertices that share edges and improving the convergence of the iterative sweep described in Section VII.

## VI. TROTTERIZATION AND NOISE MODELS

### A. First-order Trotter decomposition

The time evolution operator  $e^{-iHt}$  for the Kogut-Susskind Hamiltonian  $H = H_E + H_B$  is approximated using a first-order Trotter decomposition. The total evolution time  $T$  is divided into  $n_{\text{steps}}$  intervals of size  $dt = T/n_{\text{steps}}$ , and the evolution over each interval is approximated as

$$e^{-iH dt} \approx e^{-iH_E dt} e^{-iH_B dt}. \quad (\text{S31})$$

The Trotter error per step is  $O(dt^2 \|[H_E, H_B]\|)$ , which is controlled by choosing  $dt$  sufficiently small. For the simulations in the main text, we use  $T = 3.0$  and  $n_{\text{steps}} = 30$ , giving  $dt = 0.1$ .

Since  $H_E$  is diagonal in the Wigner basis,  $e^{-iH_E dt}$  is computed as a diagonal matrix with entries  $\exp(-i(g^2/2)j_e(j_e + 1)dt)$  for each edge. The magnetic unitary  $e^{-iH_B dt}$  is computed via direct matrix exponentiation of the  $625 \times 625$  matrix  $H_B$ .

The ideal (noiseless) evolution is obtained by iterating this Trotter step  $n_{\text{steps}}$  times starting from the strong-coupling vacuum  $|\Psi_0\rangle = |0, 0, 0\rangle^{\otimes 4}$ . The resulting sequence of states  $\{|\Psi_k\rangle\}_{k=0}^{n_{\text{steps}}}$  serves as the reference against which the noisy evolution is compared. We have verified that the Trotterized evolution preserves gauge invariance exactly:  $C^{(v)}|\Psi_k\rangle = 0$  at every vertex and every step, as required by the fact that both  $H_E$  and  $H_B$  commute with the gauge Casimir.

### B. Qudit depolarizing channel

After each Trotter step, noise is applied independently to each edge. The qudit depolarizing channel on a single  $d$ -dimensional edge ( $d = 5$  for  $j_{\text{max}} = 1/2$ ) is defined by

$$\mathcal{E}_{\text{depol}}(\rho_e) = (1 - p)\rho_e + \frac{p}{d}\mathbf{1}_d \text{Tr}(\rho_e), \quad (\text{S32})$$

where  $p \in [0, 1]$  is the error rate per edge per Trotter step. With probability  $1 - p$  the state is unchanged, and with probability  $p$  it is replaced by the maximally mixed state on the edge Hilbert space. This channel is trace-preserving and completely positive for all  $p \in [0, 1]$ .

In the full 625-dimensional Hilbert space, the depolarizing channel on edge  $e$  acts as

$$\mathcal{E}_{\text{depol}}^{(e)}(\rho) = (1 - p)\rho + \frac{p}{d}\text{Tr}_e(\rho) \otimes \mathbf{1}_e, \quad (\text{S33})$$

where  $\text{Tr}_e$  denotes the partial trace over edge  $e$  and  $\mathbf{1}_e$  is the identity on edge  $e$ . The channels on different edges commute, so the total noise channel is

$$\mathcal{E}_{\text{depol}}^{\text{total}} = \mathcal{E}_{\text{depol}}^{(e_0)} \circ \mathcal{E}_{\text{depol}}^{(e_1)} \circ \mathcal{E}_{\text{depol}}^{(e_2)} \circ \mathcal{E}_{\text{depol}}^{(e_3)}. \quad (\text{S34})$$

The depolarizing channel mixes all basis states on the affected edge, including states with different  $j$  values.

This generically creates gauge violations at both endpoints of the edge: if the edge is driven from  $j = 0$  to a mixture involving  $j = 1/2$ , the vertex coupling at both endpoints is disrupted.

For the simulations in the main text, we use error rates  $p \in \{0.001, 0.005, 0.01\}$ , which span the range of effective per-edge error rates achievable on current superconducting quantum hardware. On the latest IBM Heron processors, effective gate error rates are of order  $10^{-3}$  to  $10^{-2}$  [57], and the effective error per edge per Trotter step depends on the number of gates required to implement the step.

### C. Amplitude damping channel

The generalized amplitude damping channel models the decay of each edge toward its ground state  $|0, 0, 0\rangle$  (the  $j = 0$  singlet). This is physically motivated by energy relaxation ( $T_1$ ) processes in superconducting hardware, generalized to the qudit setting.

The channel is defined by Kraus operators on a single  $d$ -dimensional edge:

$$K_0 = |0\rangle\langle 0| + \sqrt{1-\gamma} \sum_{i=1}^{d-1} |i\rangle\langle i|, \quad (\text{S35})$$

$$K_i = \sqrt{\gamma} |0\rangle\langle i|, \quad i = 1, \dots, d-1, \quad (\text{S36})$$

where  $|0\rangle = |0, 0, 0\rangle$  is the  $j = 0$  state,  $|i\rangle$  for  $i = 1, \dots, 4$  are the four  $j = 1/2$  states, and  $\gamma \in [0, 1]$  is the damping rate per edge per Trotter step. The operator  $K_0$  preserves the  $j = 0$  population and attenuates the  $j = 1/2$  amplitudes by  $\sqrt{1-\gamma}$ , while  $K_i$  transfers population from the  $i$ -th excited state to  $|0, 0, 0\rangle$ .

One can verify the trace-preservation condition

$$K_0^\dagger K_0 + \sum_{i=1}^{d-1} K_i^\dagger K_i = \mathbf{1}_d. \quad (\text{S37})$$

In the full Hilbert space, the amplitude damping channel on edge  $e$  is applied via

$$\mathcal{E}_{\text{AD}}^{(e)}(\rho) = \sum_{k=0}^{d-1} (K_k \otimes \mathbf{1}_{\bar{e}}) \rho (K_k \otimes \mathbf{1}_{\bar{e}})^\dagger, \quad (\text{S38})$$

where  $\mathbf{1}_{\bar{e}}$  is the identity on all edges other than  $e$ . The channels on different edges are applied sequentially.

Unlike the depolarizing channel, amplitude damping has a preferred direction: it drives each edge toward  $j = 0$ . This creates gauge violations when the ideal evolved state has edges in  $j = 1/2$  coupled to singlets at the vertices; the damping can decouple the vertex by collapsing one edge to  $j = 0$  while its partner remains at  $j = 1/2$ . However, the strong coherent component of  $K_0$  (which attenuates without collapsing) also systematically drains population from the physically relevant excited configurations back toward the strong-coupling vacuum

$|0, 0, 0\rangle^{\otimes 4}$ . This effect produces a gauge-invariant error (since the vacuum is gauge-invariant) that is invisible to the gauge syndrome. For the simulations in the main text, we use damping rates  $\gamma \in \{0.001, 0.005, 0.01\}$ .

## VII. ITERATIVE GAUGE COOLING CONVERGENCE

As described in Step 5 of the main text, the recovery operation at a single vertex modifies the edge spins on the edges incident to that vertex. Because neighboring vertices share edges, a recovery at one vertex can introduce gauge violations at its neighbors. A single pass of gauge cooling over all four vertices of the plaquette is therefore insufficient to restore gauge invariance globally. In this section we characterize the convergence of the iterative sweep.

We define the gauge-invariant (GI) overlap as the average probability that each vertex is found in the singlet sector:

$$\mathcal{F}_{\text{GI}}(\rho) = \frac{1}{|V|} \sum_{v \in V} \text{Tr}(\Pi_0^{(v)} \rho), \quad (\text{S39})$$

where  $\Pi_0^{(v)}$  is the projector onto the  $J_v = 0$  sector at vertex  $v$ . A state that is exactly gauge-invariant at every vertex has  $\mathcal{F}_{\text{GI}} = 1$ . In the simulations, the iterative sweep is terminated when  $\mathcal{F}_{\text{GI}} > 1 - \epsilon$  for a tolerance  $\epsilon = 10^{-5}$ , or after a maximum of 10 sweeps.

To study convergence, we prepare the strong-coupling vacuum, apply one Trotter step, apply depolarizing noise with  $p = 0.005$  on all four edges, and then perform repeated sweeps of gauge cooling. Each sweep consists of syndrome extraction and recovery at vertices  $v_0, v_1, v_2, v_3$  in sequence. After each sweep, we compute  $\mathcal{F}_{\text{GI}}$ .

The results are shown in Table S1. After a single sweep, the GI overlap increases modestly from 0.992 to 0.993, reflecting the fact that each vertex correction partially disrupts its neighbors. Subsequent sweeps reduce the gauge-violating component geometrically, with a contraction factor of approximately 0.45 per sweep. After 5 sweeps, the deficit  $1 - \mathcal{F}_{\text{GI}}$  has decreased by roughly an order of magnitude from its initial value.

The geometric convergence can be understood as follows. Each sweep of gauge cooling is a completely positive, trace-preserving (CPTP) map  $\mathcal{E}_{\text{GC}}$  on the full density matrix. The gauge-invariant subspace  $\mathcal{H}_{\text{phys}}$  is a fixed point of this map: if  $\rho$  is supported entirely on  $\mathcal{H}_{\text{phys}}$ , then  $\mathcal{E}_{\text{GC}}(\rho) = \rho$ . The gauge-violating component of  $\rho$  is reduced by each sweep, with the reduction factor governed by the spectral gap of  $\mathcal{E}_{\text{GC}}$  restricted to the orthogonal complement of  $\mathcal{H}_{\text{phys}}$ . For the single-plaquette geometry, the observed contraction factor of 0.45 indicates a spectral gap of approximately 0.55, confirming that the map is contracting but not strongly so.

The number of sweeps required for convergence is expected to depend on the lattice size and connectivity. On

Sweep	$\mathcal{F}_{\text{GI}}$	$1 - \mathcal{F}_{\text{GI}}$
0 (before cooling)	0.992	$8.0 \times 10^{-3}$
1	0.993	$7.0 \times 10^{-3}$
2	0.9957	$4.3 \times 10^{-3}$
3	0.9977	$2.3 \times 10^{-3}$
4	0.9988	$1.2 \times 10^{-3}$
5	0.9994	$5.5 \times 10^{-4}$
6	0.9997	$2.5 \times 10^{-4}$
7	0.9999	$1.2 \times 10^{-4}$
8	0.99995	$5.2 \times 10^{-5}$
9	0.99998	$2.3 \times 10^{-5}$
10	0.99999	$1.0 \times 10^{-5}$

TABLE S1. Gauge-invariant overlap after each sweep of iterative gauge cooling, for a single Trotter step with depolarizing noise  $p = 0.005$  on the single-plaquette geometry. The deficit decreases geometrically with a contraction factor of approximately 0.45 per sweep.

larger lattices, information about gauge violations must propagate across shared edges, and the convergence rate will be related to the mixing properties of the sweep. This is analogous to the convergence of iterative gauge fixing in classical lattice gauge theory, where Landau gauge is imposed by sweeping over vertices and maximizing a local functional, with the number of sweeps growing polynomially with the linear lattice size [58, 59]. A systematic study of the scaling of the sweep count with lattice size is left to future work.

## VIII. KNILL-LAFLAMME ANALYSIS AT COORDINATION-4 VERTICES

The single-plaquette demonstration in the main text uses coordination-2 vertices, where the singlet multiplicity is  $\mu_0 = 1$  and gauge cooling constitutes trivial (exact) error correction within each edge-spin block. On larger lattices with square or higher topology, vertices have coordination number 4 or greater, and the singlet multiplicity grows beyond 1. The physical subspace at such a vertex carries nontrivial degrees of freedom, and the question of whether gauge cooling can protect those degrees of freedom becomes substantive. In this section we answer that question for the simplest nontrivial case: a single coordination-4 vertex with four spin-1/2 edges.

### A. The physical subspace encodes a logical qubit

Consider a single vertex  $v$  with four incident edges, each carrying spin  $j_{\text{max}} = 1/2$ . The gauge transformation at  $v$  acts on the tensor product of the four spin-1/2 representations contributed by these edges. Since we are interested only in the indices that transform under the gauge group at  $v$ , the relevant Hilbert space is

$(V_{1/2})^{\otimes 4} \cong (\mathbb{C}^2)^{\otimes 4}$ , which is 16-dimensional.

To decompose this space into sectors of definite total angular momentum  $J$ , we choose the coupling scheme (12)(34)  $\rightarrow J$ : first couple edges 1 and 2 to an intermediate spin  $j_{12} \in \{0, 1\}$ , then couple edges 3 and 4 to  $j_{34} \in \{0, 1\}$ , and finally couple  $j_{12}$  and  $j_{34}$  to the total  $J$ . The result is the standard Clebsch-Gordan decomposition

$$\left(\frac{1}{2}\right)^{\otimes 4} \cong 0^2 \oplus 1^3 \oplus 2^1, \quad (\text{S40})$$

where the superscripts denote multiplicities. This decomposition does not depend on the coupling order; a different scheme such as (13)(24)  $\rightarrow J$  would yield the same multiplicities but label the states differently (related by Racah recoupling coefficients).

The singlet sector  $J = 0$  has multiplicity  $\mu_0 = 2$ , so the physical subspace at this vertex is two-dimensional. The two singlet states correspond to the intermediate spin assignments  $(j_{12}, j_{34}) = (0, 0)$  (both pairs form singlets) and  $(j_{12}, j_{34}) = (1, 1)$  (both pairs form triplets that then couple to a total singlet).

The  $J = 1$  sector has multiplicity  $\mu_1 = 3$ , with the three channels labeled by  $(j_{12}, j_{34}) = (0, 1), (1, 0), (1, 1)$ . Together with  $2J + 1 = 3$  magnetic substates, this gives  $3 \times 3 = 9$  states. The  $J = 2$  sector has  $\mu_2 = 1$ , giving  $2J + 1 = 5$  states. The total is  $2 + 9 + 5 = 16$ , consistent with the dimension of  $(\mathbb{C}^2)^{\otimes 4}$ .

### B. How single-qubit errors transform under the gauge group

To understand which errors the gauge syndrome can detect, we need to know how single-qubit errors transform under  $\text{SU}(2)$ . Any operator on a single spin-1/2 edge decomposes into irreducible spherical tensor components under the adjoint action of the gauge group. The space of all  $2 \times 2$  matrices is 4-dimensional and decomposes as  $V_{1/2} \otimes V_{1/2} \cong V_0 \oplus V_1$ : a one-dimensional scalar ( $J = 0$ ) piece and a three-dimensional vector ( $J = 1$ ) piece. The scalar piece is the identity matrix  $\mathbf{1}_2$  (the unique operator commuting with all  $\text{SU}(2)$  transformations, by Schur's lemma). The vector piece is the three-dimensional space of traceless Hermitian matrices, spanned by the Pauli matrices  $\{X, Y, Z\}$ .

Since the Pauli matrices are traceless, a single-qubit Pauli error  $P \in \{X, Y, Z\}$  on edge  $k$  is purely  $J = 1$  and maps the singlet sector entirely into the  $J = 1$  sector. The identity component of any error channel acts trivially on the codespace and requires no correction.

The previous argument establishes that any single-qubit Pauli error takes the singlet into the  $J = 1$  sector, but the  $J = 1$  sector has three magnetic substates ( $M = -1, 0, +1$ ). To determine which substate the error produces, we re-express the Pauli matrices in the spherical tensor basis, whose elements have definite magnetic

quantum number  $q$ :

$$O_0^{(1)} = Z, \quad O_{\pm 1}^{(1)} = \mp \frac{1}{\sqrt{2}}(X \pm iY). \quad (\text{S41})$$

When a spherical tensor with component  $q$  acts on a singlet ( $M = 0$ ), the selection rule  $\Delta M = q$  determines the magnetic quantum number of the output state:

- $Z$ , being the  $q = 0$  component, maps the singlet sector into  $M = 0$  of  $J = 1$ .
- $X$  and  $Y$ , being linear combinations of the  $q = \pm 1$  components, map the singlet sector into the span of the  $M = \pm 1$  subspaces of  $J = 1$ .

This decomposition by  $M$  sector is essential for the Knill-Laflamme analysis and residual error characterization that follow, because errors landing in different  $M$  sectors produce different syndromes and are handled by different recovery operations.

No single-qubit error can reach  $J = 2$ , because the operator space on a single spin-1/2 decomposes as  $0 \oplus 1$  and therefore cannot induce  $J = 2$  transitions. Two-qubit errors, acting on two edges simultaneously, can reach  $J = 2$ .

### C. Every single-qubit error is detected

We now prove the central detection result. Consider a single-qubit Pauli error  $P \in \{X, Y, Z\}$  acting on edge  $k$ , with the identity on the remaining three edges. We denote this operator  $P_k \otimes \mathbf{1}_{\bar{k}}$ , where  $k$  refers to all edges other than  $k$ . The singlet-to-singlet block of this operator vanishes identically:

$$\Pi_0 (P_k \otimes \mathbf{1}_{\bar{k}}) \Pi_0 = 0 \quad (\text{S42})$$

for all  $P \in \{X, Y, Z\}$  and all edges  $k \in \{0, 1, 2, 3\}$ , where  $\Pi_0$  is the projector onto the singlet sector at the vertex.

This follows directly from the representation theory. As shown above, any operator on a single spin-1/2 edge decomposes into a scalar ( $J = 0$ ) component proportional to the identity and a vector ( $J = 1$ ) component. The Wigner-Eckart theorem requires that the singlet-to-singlet matrix element of a rank- $J$  tensor vanishes unless  $J = 0$ . Since Pauli operators are traceless, they are purely  $J = 1$  and have no scalar component. Their singlet-to-singlet matrix elements therefore vanish identically.

The physical consequence is that every single-qubit error necessarily produces a gauge violation ( $J \neq 0$ ) and is therefore detected by the syndrome extraction. This is a strong property: the gauge code detects all single-qubit errors at a coordination-4 vertex.

### D. Distinct errors can have the same syndrome

Detection is not the same as correction. For correction, we would need to identify *which* error occurred. This is

where the multiplicity structure creates an obstruction. For each single-qubit error on edge  $k$  mapping the singlet sector ( $\mu_0 = 2$ ) to the  $J = 1$  sector ( $\mu_1 = 3$ ), the action decomposes as  $E = O_N^{(1)} \otimes A_k$ , where  $O_N^{(1)}$  carries the gauge quantum numbers and  $A_k : \mathbb{C}^2 \rightarrow \mathbb{C}^3$  acts on the multiplicity space. The gauge syndrome ( $J, M, N$ ) determines  $O_N^{(1)}$  completely but tells us nothing about  $A_k$ , which depends on which edge the error acted on.

We have computed  $A_k$  explicitly for all four edges and all three Pauli types. The key structural features are:

1. All  $A_k$  matrices have singular values  $(1, 1)$  when expressed in the spherical tensor basis. Equivalently, the Cartesian Pauli errors  $X$  and  $Y$ , which are superpositions of the  $q = \pm 1$  components with coefficient  $1/\sqrt{2}$ , yield singular values  $(1/\sqrt{2}, 1/\sqrt{2})$  when projected onto a definite  $M$  sector.
2. Errors on different edges produce different  $A_k$  matrices. Edges within the same pair in the (12)(34) coupling scheme (edges 0 and 1, or edges 2 and 3) produce  $A_k$  matrices that differ only by sign flips, reflecting their symmetric role in the first-stage coupling. Edges from different pairs (e.g., edges 0 and 2) produce  $A_k$  matrices with nonzero entries in different positions, reflecting the fact that they participate in different stages of the coupling. This structural distinction is what causes the off-diagonal Knill-Laflamme products  $A_k^\dagger A_l$  to deviate from the identity.

### E. The Knill-Laflamme conditions fail

The Knill-Laflamme conditions for exact quantum error correction, conditioned on a fixed syndrome sector, reduce to the requirement that for any two errors  $E_a$  and  $E_b$  within that sector,

$$A_a^\dagger A_b \propto \mathbf{1}_{\mu_0}. \quad (\text{S43})$$

If this holds, the recovery can undo the error without disturbing the logical qubit encoded in the multiplicity space.

The diagonal terms  $A_k^\dagger A_k$  are proportional to  $\mathbf{1}_2$  for every edge  $k$  and every Pauli type. This is necessary but not sufficient. The off-diagonal terms  $A_k^\dagger A_l$  for  $k \neq l$  are generically *not* proportional to  $\mathbf{1}_2$ . For example, for  $Z$  errors on edges 0 and 1,

$$A_0^\dagger A_1 = \begin{pmatrix} -1 & 0 \\ 0 & \frac{1}{3} \end{pmatrix}, \quad (\text{S44})$$

which is manifestly not proportional to the identity. For cross-pair edges (e.g.,  $k = 0, l = 2$ ), the product has off-diagonal entries as well. The Knill-Laflamme conditions are therefore violated. Different edges produce the same gauge syndrome but act distinguishably on the multiplicity space. No syndrome-based recovery can perfectly undo all single-qubit errors.

## F. What the residual errors look like

After gauge cooling, the state is returned to the singlet sector, but the recovery cannot distinguish which edge caused the error. The result is a residual logical error on the 2-dimensional multiplicity space  $\mathbb{C}^{\mu_0} = \mathbb{C}^2$ .

To characterize these residual errors, we fix a reference recovery (the pseudoinverse of the error map from edge 0) and compute the effective  $2 \times 2$  operator  $R \cdot A_k$  for each edge  $k$ . Decomposing into Pauli components, we find the following structure for the  $M = 0$  sector ( $Z$  errors):

Error	$I$ weight	$X$ weight	$Z$ weight
$Z_0$	1.00	0	0
$Z_1$	0.20	0	0.80
$Z_2$	0.20	0.60	0.20
$Z_3$	0.20	0.60	0.20

Here the weights are  $|c_P|^2 / \sum_{P'} |c_{P'}|^2$ , where  $c_P$  is the coefficient of Pauli  $P$  in the decomposition of  $R \cdot A_k$ . The  $M = \pm 1$  sectors ( $X$  and  $Y$  errors) exhibit the same pattern.

The key features are:

1. The reference edge (edge 0) is perfectly corrected: the residual is proportional to the identity.
2. The paired edge (edge 1) produces a residual that is predominantly Pauli  $Z$  on the multiplicity qubit.
3. The cross-pair edges (edges 2 and 3) produce residuals that are a mixture of Pauli  $X$  and  $Z$ .
4. No residual  $Y$  component appears for any single-qubit error.

The absence of  $Y$  errors and the bounded weights of  $X$  and  $Z$  errors suggest compatibility with CSS-type concatenation. An  $[[n, 1, d]]$  CSS code encoding the multiplicity qubit across  $n$  vertices could correct these residuals, implementing a two-layer error correction scheme consisting of gauge cooling to eliminate gauge-variant errors, followed by a stabilizer code to correct the residual multiplicity-space distortions. We leave the implementation of this concatenated scheme to future work.